

1

2

Spatial intensity distribution in plasmonic particle array lasers

3

Ke Guo¹ and A. Femius Koenderink¹

4

¹*Center for Nanophotonics, AMOLF, Science Park 104,*

5

1098 XG Amsterdam, The Netherlands

6

(Dated: December 18, 2018)

Abstract

We study spatial intensity distributions in plasmonic distributed feedback lasers (DFB) composed of metal nanoparticle arrays. Real-space distributions give direct access to "coupling strength" parameters that quantify DFB performance in the framework of coupled wave theory (CWT). We observe that CWT indeed parametrizes real space intensity distributions, and extract coupling strength parameters that quantify the plasmonic feedback mechanism. These coupling strength parameters differ from those required to parameterize the plasmonic band structures of the system, counter to the common result for dielectric DFB lasers, where CWT describes both real space and k-space physics. Also, measured coupling constants are significantly smaller than would be expected from estimates on basis of the unit cell geometry. We conclude that while CWT is successful as a generic description of any system with forward and backward waves with gain, matching this model to photonic band structures, or to common parameter estimate approaches, fails because the underlying assumption that a perturbative plane wave expansion applies is not valid for plasmonic antenna arrays.

7 INTRODUCTION

8 Currently there is a large interest in collective light-matter interaction effects in periodic reso-
9 nant scattering systems, such as plasmonic antenna arrays and dielectric metasurfaces [1]. Diffrac-
10 tive plasmonic antenna arrays provide strong field confinement, owing to the plasmonic nature of
11 constituent scatterers in the unit cell, yet compared to single plasmon nano-antennas they yield
12 higher quality factors and concomitantly lower absorption loss. As reviewed by Lozano et al. [2],
13 this poses significant advantages for solid-state lighting. Recently, several groups noted that such
14 structures are also of large interest for effects beyond fluorescence control (cooperative emission),
15 including plasmon antenna array lasers [3–16], strong coupling between dense emitter ensembles
16 and plasmon antenna arrays [17, 18], plasmon-exciton-polariton lasing [13], and Bose-Einstein
17 condensation of exciton-polaritons [19]. In a separate development, there is a rising interest in
18 dielectric lasing metasurfaces with resonant building blocks as lossless alternatives to plasmonic
19 arrays [20]. In all these efforts, there is a large need to quantitatively understand the emergence
20 of cooperative emission, accounting at the same time for the periodicity, the strongly resonant
21 properties of the unit cell, and finite-sized effects in finite system realizations. Currently, this is
22 far beyond standard numerical approaches. For instance, full-wave numerical approaches for plas-
23 mon systems are only feasible with either periodic boundary conditions (full unit cell resolution,
24 no finite-system effects), or for real-space domains that are too small to encompass a realistic
25 number of system unit cells (finite-system, but hardly recognizable as periodic).

26 In this work we focus on plasmon antenna array lasers which are the most well-studied exam-
27 ple of the abovementioned systems. Diffractive plasmon lasers [3–16] were first considered as
28 potential realizations of the plasmon spaser [21] with a better tradeoff[22] between confinement
29 and loss than single nanoparticle/nanowire realizations[23–34]. Diffractive plasmonic structures
30 with gain are akin to distributed feedback (DFB) lasers [35–40]. Lasing of these systems oc-
31 curs near geometric Bragg conditions, and is strongly directional with thresholds similar to those
32 of polymer DFB lasers. At the same time, they have much larger interaction strength than con-
33 ventional dielectric DFB lasers owing to the strong resonant scattering cross section of plasmon
34 antennas. This is apparent in the wide stop gaps measured in plasmon lattice band structures [41].
35 To understand such plasmon antenna array lasers, the group of Odom notably focused on Purcell
36 enhancement due to strong field confinement [8–11], which is particularly relevant for intrinsically
37 low quantum-efficiency gain media. In a different realization using efficient instead of inefficient

38 dyes, Schokker et al.[42] have claimed that plasmon particle array lasers also stand out for strong
39 feedback from resonant scattering, which makes them extraordinary robustness to disorder. While
40 the underlying plasmon band structure in both these realizations was studied in depth, these works
41 did not address quantitatively in real space how particle array plasmon lasers compare to conven-
42 tional DFB lasers based on dielectric or loss/gain gratings.

43 In this article, we study finite-sized plasmon particle array lasers and quantitatively compare
44 their properties to coupled wave predictions. As these lasers are qualitatively akin to DFB lasers
45 in their characteristics, Our aim is to examine whether coupled wave theory (CWT) developed by
46 Kogelnik and Shank [43] can offer an accurate description of these systems, and therefore form
47 a strong basis to describe active dielectric metasurfaces and cooperative phenomena in plasmon
48 antenna arrays beyond lasing. Good agreement between CWT and experiments was demonstrated
49 for metal hole array lasers [4, 5], which however have weak and nonresonant perturbations (the
50 air holes). To benchmark if this premise holds also for resonant antenna array systems, it is im-
51 portant to perform quantitative instead of qualitative comparisons. In this work, we determine
52 coupling strengths from measured spatial intensity distributions of lasing modes in plasmon parti-
53 cle arrays as function of the detuning of the lasing condition from the particle plasmon resonance.
54 By comparing fitted coupling strengths with calculations and measured band structure parameters,
55 we answer two questions: (i) whether the CWT meant for weakly scattering systems applies to
56 plasmonic lattices in terms of parameterizing spatial intensity distributions, and if so, (ii) how
57 the plasmon resonance near the lasing condition influences the apparent coupling strength, and
58 bandstructure.

59 I. CWT FOR DFB LASERS

60 This section summarizes those aspects of CWT required to describe our experiments. CWT
61 was developed by Kogelnik and Shank in 1972 to describe one dimensionally (1D) periodic DFB
62 lasers [43], and was later further extended to different 1D and 2D DFB laser geometries [44–47].
63 In CWT, a DFB laser is described as a waveguide with a weakly scattering periodic perturbation
64 in its optical constant which leads to coupling between forward and backward propagating in-
65 plane waves [43, 44] by Bragg diffraction. These waves furthermore experience gain and are
66 subject to outcoupling loss, also due to Bragg diffraction. Reported plasmon lattice lasers are
67 usually 2D periodic structures, with resonant nano-antennas assembled in a 2D lattice. To derive

68 CWT for 2D systems, the starting point is a plane wave expansion method to solve for the in-
 69 plane amplitude distribution of modes that are understood to have a vertical mode profile and
 70 mode index n_{WG} taken from the uncorrugated 2D waveguide solution. The periodic corrugation
 71 is incorporated as a small perturbation that couples the waves through coupling constants $\kappa(\mathbf{G})$,
 72 where the set \mathbf{G} refers to the reciprocal lattice vectors. The coupling constants are determined by
 73 the 2D Fourier transform of the unit cell corrugation, weighted with the finite overlap of the vertical
 74 waveguide mode profile [44]. For our system, the coupling constants have complex values. Real
 75 and imaginary coupling constants are commonly understood for DFB lasers as index-coupling and
 76 gain (or loss) coupling respectively.

77 While periodic potentials in principle couple all plane wave components of any Ansatz solution
 78 written as a Bloch wave expansion, the essence of CWT is that only a small subset of plane
 79 waves and \mathbf{G} 's needs to be considered, namely only those that allow standing waves by the Bragg
 80 diffraction. Following the model for 2D lattices presented in Ref. [45], this means only those waves
 81 should be retained with in plane momentum $|\mathbf{k} + \mathbf{G}| = \omega/cn_{\text{WG}} = \beta$, with optical frequency ω in
 82 the gain window of our lasing medium. The philosophy of our work is to extract coupling
 83 constants κ by comparing measured spatial intensity profiles that are predicted by CWT. Since for
 84 square lattices predicted profiles are quite complex [45], we focus on 2D arrays with a rectangular
 85 geometry instead of a square geometry. The pitches a_x and a_y are designed to be different by about
 86 15%, such that Bragg conditions in the x and y direction can not be simultaneously met and only the
 87 waves in the y direction couple within the narrow frequency window of the laser gain. Retaining
 88 only those Bragg conditions, the 2D model reduces to the 1D CWT, with coupling coefficients κ
 89 calculated from the 2D unit cell geometry. In this 1D CWT, the light field is reduced to the sum
 90 of two counter propagating waves $S(y)e^{iG_y y}$ and $R(y)e^{-iG_y y}$ travelling in the $-y$ and y directions
 91 that are coupled through the first and second order Bragg diffractions (Fig. 1(a)). Lasing operation
 92 is expected near the second order Bragg diffraction, at wave vector near $G_y = 2\pi/a_y$, with a_y the
 93 lattice constant in the y direction. The slowly varying envelopes $R(y)$ and $S(y)$ satisfy [44]

$$-\partial_y R(y) + \left[\frac{g}{2} - \frac{i}{2G_y} \left(n_{\text{wg}}^2 \left(\frac{\omega}{c} \right)^2 - G_y^2 \right) - \kappa_{\text{out}} \right] R(y) - (i\kappa_{\text{back}} + \kappa_{\text{out}})S(y) = 0, \quad (1a)$$

$$\partial_y S(y) + \left[\frac{g}{2} - \frac{i}{2G_y} \left(n_{\text{wg}}^2 \left(\frac{\omega}{c} \right)^2 - G_y^2 \right) - \kappa_{\text{out}} \right] S(y) - (i\kappa_{\text{back}} + \kappa_{\text{out}})R(y) = 0. \quad (1b)$$

94 Here κ_{back} quantifies the coupling strength responsible for feedback through second order Bragg
 95 diffraction ($\mathbf{G} = (0, 4\pi/a_y)$), and κ_{out} for the coupling between guided waves and out of plane

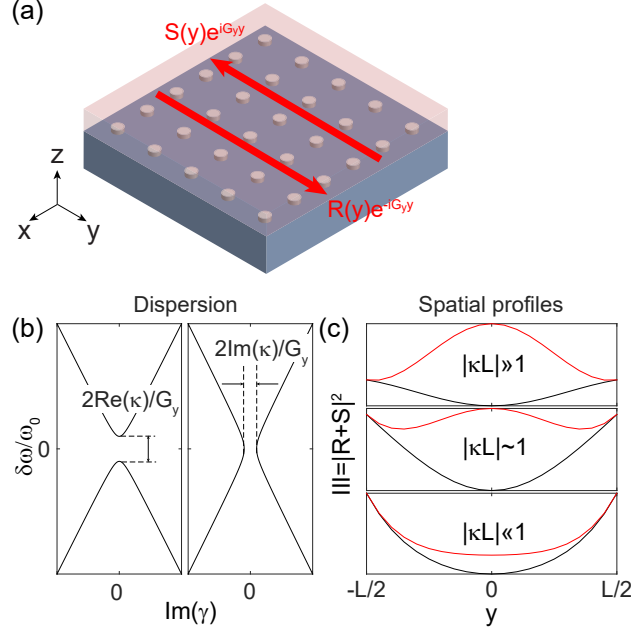


FIG. 1. (a) Sketch of a plasmon DFB laser based on a rectangular lattice of Ag nanoparticles. Feedback only occurs in the y -direction (b) canonical photonic band diagram of CWT, with $\kappa_{\text{back}} \gg \kappa_{\text{out}}$. The real (imaginary) part of the coupling coefficient results in a band gap in frequency (wave vector). (c) canonical intensity profiles of out-coupled lasing mode (lowest threshold) in under-coupled, critically coupled and over-coupled regimes (bottom to top). Red (black) indicate (anti)-symmetric combinations $|R \pm S|^2$.

96 radiation through first order Bragg diffraction ($\mathbf{G} = (0, 2\pi/a_y)$). We further define $\kappa = \kappa_{\text{back}} -$
 97 $i\kappa_{\text{out}}$.

98 Following Ref. [43, 44], the above equations provide the below-threshold band structure and the
 99 above-threshold real space intensity distribution. Fig. 1(b) illustrates two typical types of below-
 100 threshold band structures. The coupling between the two waves opens a band gap at the crossing
 101 of the two waveguide modes at $k_y = 0$ and $\omega_0 = cG_y/n_{\text{wg}}$. When $|\text{Re}\kappa| \gg |\text{Im}\kappa|$, the photonic
 102 bands split at $k_y = 0$ with a gap in frequency, with $\delta\omega = \omega - \omega_0 \approx \frac{\omega_0}{G_y}(-i\kappa_{\text{out}} \pm \kappa)$. The stop gap
 103 is symmetric around the Bragg condition ω_0 as long as $|\kappa_{\text{back}}| \gg |\kappa_{\text{out}}|$, i.e., unless radiation loss
 104 is strong (Fig. 1(b, left)). If $|\text{Re}\kappa| \ll |\text{Im}\kappa|$ (gain/loss coupling), the photonic bands split in wave
 105 vector rather than in frequency as shown in Fig. 1(a, right).

106 The above-threshold real space profiles have the following form (array of overall dimension L)

$$R(y) = \sinh\gamma(y + \frac{1}{2}L), \quad \text{and} \quad S(y) = \pm \sinh\gamma(y - \frac{1}{2}L), \quad (2)$$

107 where γ and the threshold gain g_{thr} satisfy

$$\pm i\gamma/\sinh\gamma L = \kappa \quad \text{and} \quad g_{\text{thr}} = 2\text{Re}(\gamma\coth\gamma L + \kappa_{\text{out}}). \quad (3)$$

108 The slowly varying envelopes determine the output spatial intensity distribution obtained when
 109 imaging the laser with far field optics. In a purely scalar model the intensity of the two waves
 110 outcoupled by the lattice through the first order Bragg diffraction add up as $|R + S|^2$. Once polar-
 111 ization is included in the model, for samples supporting a TE (TM) waveguide mode it is important
 112 to realize that detection polarization along x (y) selects $|R + S|^2$, while cross-polarized detection
 113 results in a signal proportional to $|R - S|^2$.

114 Fig. 1(b) shows examples of $|R + S|^2$ for various combinations of array size L and coupling
 115 constant κ . Depending on the sign in Eq. (2), the outcoupled waves present either constructive
 116 or destructive interference, resulting in bright (antinodes on the particles) and dark (nodes on the
 117 particles) modes. Dark modes (black lines) have zero emission intensity in the center of the array
 118 yet high intensity on the edges. A bright mode (red lines) has a spatial profile dependent on the
 119 product of the coupling strength κ and overall array size L , which can be classified into three
 120 regimes: under-coupled, critically coupled and over-coupled. When $|\kappa L| \ll 1$ (under-coupled),
 121 the emission profile of the first lasing mode will essentially report on the sinh tails in Eq. (2),
 122 meaning bright emission only from the array edges. As $|\kappa|$ increases, the laser transitions from
 123 critically coupled to over-coupled ($|\kappa L| \gg 1$), and the emission in the center increases.

124 To conclude, CWT simultaneously predicts below-threshold photonic dispersion diagrams with
 125 characteristic stop gaps, and above-threshold real-space intensity distributions, both parametrized
 126 by the *same* coupling strength parameters κ . These parameters should be expected to systemat-
 127 ically vary with the plasmon particle resonance. In this spirit, we seek to determine the relation
 128 between coupling strength (κ) and the plasmon response from spatial intensity distributions for
 129 different array sizes (varying L) and particles sizes.

130 II. EXPERIMENTAL SETUP AND SAMPLE GEOMETRY

131 We perform measurements in an inverted fluorescence microscope equipped with real space and
 132 back focal plane (Fourier-space) imaging, as well as spectral (Fourier) imaging, using a modified
 133 version of the setup of Ref [12], cf. Fig. 2 (a). To obtain a large field of view we use a Nikon L
 134 PLAN, 50 \times , NA=0.7 objective. We pump and collect through the substrate side, employing single

532 nm wavelength, 0.5 ps pulses (Teem Photonics, type STG-03E-1S0), with a beam diameter of $\sim 120 \mu\text{m}$ on the sample and pulse energy up to $\sim 1 \mu\text{J}$. The pulse energy is controlled by an acousto-optic modulator (AOM). To avoid any polarization anisotropies, we convert the pump polarization to circular and use a beam splitter ($R=80\%$) as opposed to a dichroic mirror. Emission is collected through the beam splitter and passed through a pair of Chroma HHQ545lp long pass filters to remove pump light, and directed through a $1\times$ telescope to either a thermo-electrically cooled Si CCD camera (Andor CLARA) or a Shamrock303i spectrometer (with Andor iVAC Si CCD) after tube lens of 200 mm and 100 mm respectively. The first telescope lens counted from the sample is placed at its focal distance from the back focal plane of the objective, and also works as a Fourier or 'Bertrand' lens when the second lens of the telescope is removed. When the back focal plane of the objective is imaged on the spectrometer, the entrance slit ($20 \mu\text{m}$) selects a vertical slice in the center of the Fourier image ($k_x = 0$) so that the emission intensity as a function of k_y and ω is imaged on the spectrometer camera. As demonstrated by Schokker [12], the resulting spectral images show distinct features that trace out the band structure of the sample, when operated below threshold. Similarly, in real space imaging the spectrometer slit (slit width $20 \mu\text{m}$) spatially selects a strip of width $0.8 \mu\text{m}$ on the sample. Above threshold, these techniques provide the lasing spectrum and the spatial distribution of lasing modes.

The arrays are designed to have a lattice constant of 370 nm in the y -direction. In the x -direction, the array has a much smaller lattice constant of 320 nm. Therefore, only the waveguide modes in the y and $-y$ direction can couple with each other through the Bragg diffraction of order (0,2), while out coupling occurs through the Bragg diffraction of order (0,1). As other diffraction orders do not contribute, the lasing action is essentially as in a 1D periodic DFB laser. The Ag nanoparticles were fabricated on glass cover slips using electron-beam lithography, successive thermal evaporation and lift off [12]. Each Ag nanoparticle has a height of 30 nm and a diameter that we systematically vary from 40 nm to 90 nm in different arrays. The samples are covered by spincoating a 350 nm SU8 layer doped with about 2.5 wt% Rh6G molecules, which both acts as a gain medium and as a waveguide layer. Because SU8 has a refractive index of about 1.60 (measured by ellipsometry) exceeding the index of the glass substrate ($n=1.52$), this layer supports only a fundamental TE and TM waveguide mode, with mode indices of about 1.55. Note that in this respect our lasers are fundamentally different from the plasmon particle array lasers studied in Ref. [8, 9, 13, 14] which use layer stacks there are index-matched, hence relying on surface lattice resonances instead of waveguide modes.

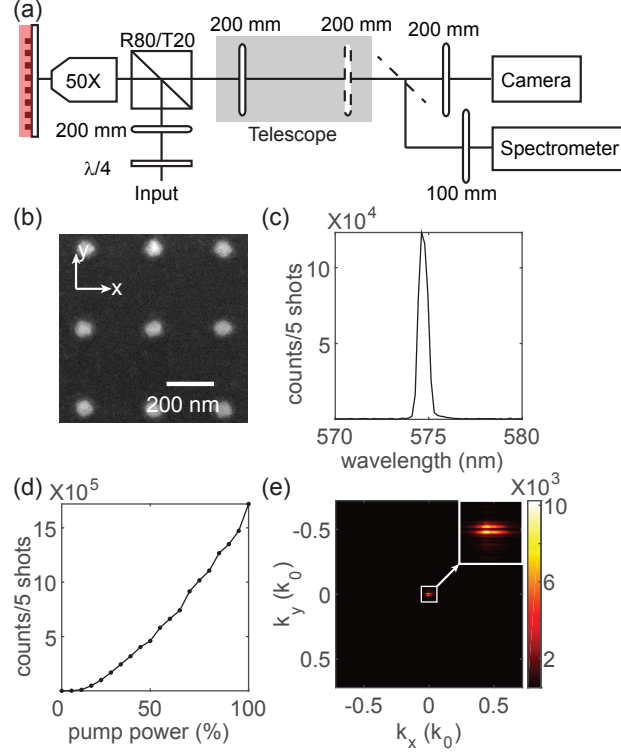


FIG. 2. (a) Schematic of the fluorescence microscope. We form either a real or Fourier space image on either a CCD or a spectrometer entrance slit. The first telescope lens (left) acts as Fourier lens when the second lens (right, dashed) is removed. (b) Scanning electron micrograph (SEM) image of 80 nm Ag particle array before depositing the gain medium. (c) Typical above-threshold emission spectrum at 50 % pump power ($80 \times 80 \mu\text{m}^2$ plasmon DFB laser with particle diameter 80 nm). (d) Corresponding threshold curve and (e) Fourier image of the x -polarized emission showing a narrow directional beam. The inset of (e) shows a zoom near $k_x = k_y = 0$.

III. CHARACTERIZATION MEASUREMENTS

Previously we reported lasing only for square arrays [12]. Therefore, we first confirm that also rectangular arrays lase. Fig. 2(c-e) show data for a $80 \times 80 \mu\text{m}^2$ rectangular lattice of Ag disks with diameter of 80 nm. When the pump intensity exceeds about 10% of the AOM range, the observed emission spectrum abruptly changes from the broad fluorescence spectrum of Rh6G to a narrow peak at around 575 nm as shown in Fig. 2 (c). The emission intensity in a narrow band (± 1.5 nm) around the lasing wavelength as function of pump power (Fig. 2 (d)) shows significantly different slopes before and after the 10 % pump power level, indicating typical threshold behavior. When crossing the threshold, the laser output furthermore shows a strong change in directivity, from a

176 Lambertian profile to a highly directional beam, as shown in Fig. 2(e). The observed bandwidth
 177 of about 1.5 nm is somewhat wider than the bandwidth of typical plasmonic DFB lasers with a
 178 square lattice studied by Schokker et al. [12] [0.6 nm, measured with the same spectrometer and
 179 grating (300 lines / mm)]. We attribute this to the presence of multiple lasing modes with slightly
 180 different wave vector and frequency, as will be discussed in the following sections.

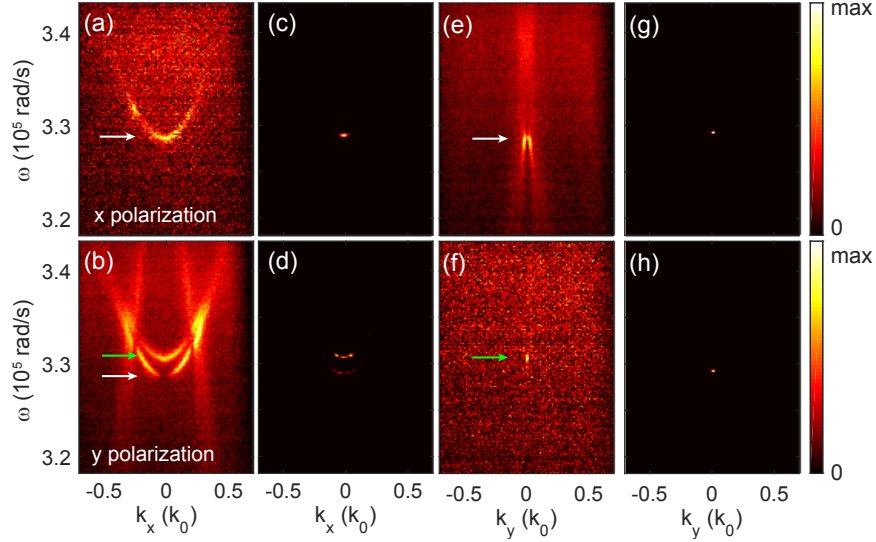


FIG. 3. Measured polarized Fourier spectra near (a-d) $k_y = 0$ and (e-h) $k_x = 0$. (a-b,e-f) below and (c-d,g-h) above threshold. (a,c,e,g): x -polarization; (b,d,f,h): y -polarization. Green arrows: TM waveguide mode; white arrows: TE. $L = 80 \mu\text{m}$, $d = 90 \text{ nm}$. (a-b, e-f) are below-threshold (data from 600 shots at 5 % pump power). (c-d,g-h) show lasing at TE and TM bandedges (OD1 neutral density filter, single-shot excitation at 100 % pump power). The maximum counts in each image are (a) 27, (b) 82, (c) 1670, (d) 3452, (e) 87, (f) 21, (g) 14526, (h) 632.

181 Spectrally resolved k -space imaging further characterizes the modes, as Fig. 3 illustrates for a
 182 representative lasing array ($L = 80 \mu\text{m}$, $d = 90 \text{ nm}$). Fig. 3(a-b) and (e-f) show below-threshold
 183 band diagrams for two different slices in k -space, i.e., at $k_y = 0$ and at $k_x = 0$ respectively, where
 184 we recall that the feedback direction for which a Bragg condition is satisfied is the y -direction. The
 185 waveguide mode dispersion folded back in k -space by first order Bragg diffraction hence appears
 186 as two anti-crossing lines in the $k_x = 0$ plane and as a parabolic band in the $k_y = 0$ plane, as shown
 187 in Fig. 3(a-b,e-f). By measuring the polarization of the banddiagram at $k_x = 0$ (Fig. 3(e-f)), we are
 188 able to separate the contributions of the TE (x -polarization) and TM (y -polarization) waveguide
 189 modes. Our data shows that both fundamental TM (marked with green arrows) and TE (marked

with white arrows) waveguide modes are supported by the sample, consistent with simple slab-waveguide dispersion calculations [48]. In Fig. 3(e-f), the TE feature appears strongest, while the TM waveguide mode leaves only a weak signature in fluorescence, consistent with the poor overlap of the TM waveguide mode (weak in-plane electric field) and the predominantly in-plane polarizability tensor of the flat disk nanoparticles.

The above-threshold images in Fig. 3(c-d) and (g-h) show that the sample lases near band edges of both TE and TM waveguide modes with two distinct frequencies. Unlike square array lasers which lase at $k_x \approx k_y \approx 0$, our rectangular array lasers lase at $k_y \approx 0$ over a range of k_x . The TM waveguide mode lases only in y polarization. This is consistent with Fig. 3(a-b), which show that TM waveguide mode is polarized in the y -direction with hardly any x -polarization components. The TE waveguide mode lasing output instead has x polarization components for all (small) k_x and additionally y polarization components for $k_x \neq 0$. Very similar behavior is observed for samples with different array sizes ($80 \times 80 \mu\text{m}^2$, $60 \times 60 \mu\text{m}^2$ and $40 \times 40 \mu\text{m}^2$) and particle diameters (40 nm to 90 nm). All the investigated arrays lase at the TE mode, with both x and y polarization components, while only arrays with big particles diameters (larger than 70 nm) show lasing at the TM waveguide mode within the range of pump intensities. In the remainder we focus on analyzing the TE mode only.

IV. SPATIAL INTENSITY DISTRIBUTION AND COUPLING STRENGTH OF PLASMON DFB LASERS

To test whether the lasers indeed have non-trivial spatial intensity distribution as predicted by CWT, we measure above threshold real space images in two detection polarization channels, as shown for a representative example in Fig. 4 [$60 \times 60 \mu\text{m}$, lasing on TE mode]. The lasing emission in both detection polarization channels show very finely spaced intensity fluctuations, i.e. speckles that have a size at the diffraction limit of our imaging system, which in itself evidences spatial coherence [42]. The speckle pattern is multiplied by a slowly varying envelope that is hardly varying in the x -direction, but shows significant contrast as function of the y coordinate. The x -polarized component has low intensity in the center ($y = 0$) and high intensity at the edges of the array, similar to either the coupled-mode prediction for an under-coupled symmetric mode, or alternatively to the profile of an asymmetric mode in any coupling strength regime. The y -polarization component has highest intensity at $y = 0$, which uniquely points to an over-coupled

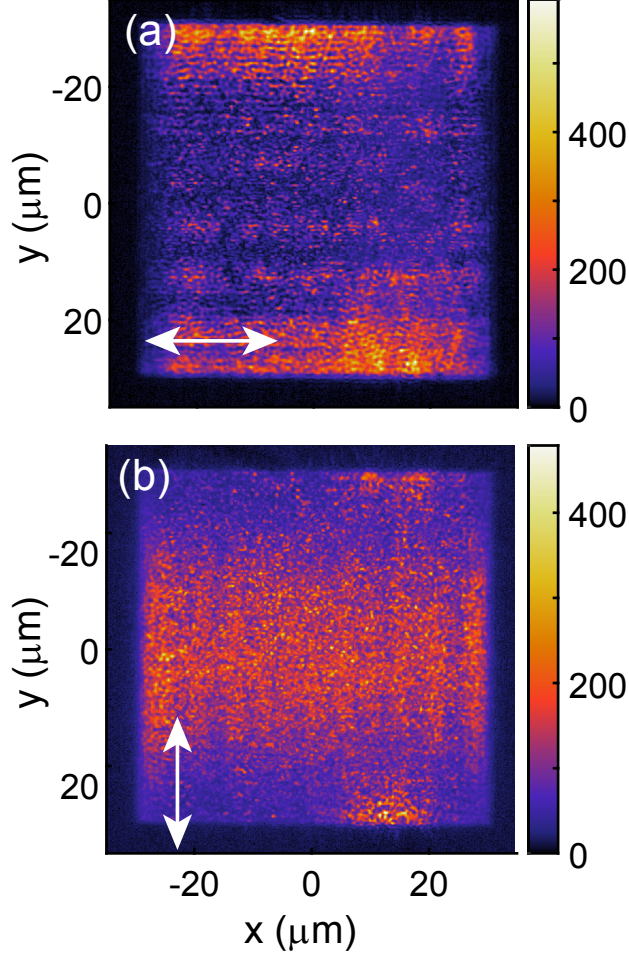


FIG. 4. Measured real space profiles of a laser with $L = 60 \mu\text{m}$, $d = 90 \text{ nm}$ in (a) x and (b) (y) polarization. Single shot, 100 % pump power.

mode.

We measure the spatial intensity distribution in the feedback direction (y -direction) for the TE modes for all our samples by imaging the lasing array onto the spectrometer slit, selecting a slice from the center ($x \approx 0$) of the array along the y -axis. The spectral dispersion of the spectrometer allows us to extract the spatial intensity distribution along the slice of sample selected by the entrance slit at any wavelength. By summing the intensity in a bandwidth within just 1 nm near the TE lasing wavelength from spectral images, we obtain the spatial intensity distribution in the y -direction for the two polarizations of the TE mode. Selecting this small wavelength range also rules out any significant contribution of spontaneous emission, as the fluorescence spectrum of Rh6G has a width above 60 nm. Fig. 5(a-b) shows measured spatial intensity distributions from samples with different particle sizes and field sizes for both detection polarization channels. Apart

231 from the sub-micron intensity fluctuation (speckles), the x - and y -polarization components have
 232 distinctively different envelope functions. In all cases, the x -polarized laser emission has near-
 233 zero intensity (given the noise floor of our single shot CCD images) in the center of the sample
 234 and highest intensity at the edges as shown in Fig. 5 (a). On the other hand, the y -polarized emis-
 235 sion (Fig. 5 (b)) shows a clear transition from an under-coupled profile with low intensity in the
 236 center from arrays with small width (bottom row) or small particles (right column), to critically
 237 coupled profiles (center row and center column), and eventually to an over-coupled profile with
 238 intensity higher in the center than at the edges as the array width and particle diameter increase to
 239 80 μm and 90 nm (top left). Therefore, we conclude that the TE lasing mode is an antisymmetric
 240 combination of forward and backward waves, which in the far field carries over to an antisymmet-
 241 ric x -polarization component and a symmetric y -polarization signature. This assignment agrees
 242 with the conclusion in Ref. [49] that the lasing of the TE mode occurs at the band edge where
 243 the nodes of the standing wave formed by the counter propagating TE modes are at the nanoparti-
 244 cles, which is the configuration that minimizes absorption and radiation losses. These results are
 245 also consistent with the lasing profiles measured by Hakala et al. [14]. In Ref. [14], Hakala et al.
 246 claimed to observe lasing at two opposing stop band edges, with a "dark" mode with low intensity
 247 in the center of the array and a "bright" mode with high intensity in the center. We note that strictly
 248 their observation neither provides a unique symmetry assignment which requires polarization res-
 249 olution, nor is unique for plasmonic "bright" dipole and "dark" quadrupole moments. Instead,
 250 these spatial profiles can occur for dielectric and plasmonic lasers alike according to CWT. Thus
 251 the apparent signature of being dark in the center of the array can be observed at both "dark" and
 252 "bright" dispersion branches, depending on the detection polarization with respect to the dominant
 253 lasing polarization, and not exclusively indicative of whether the laser operates in under-coupled
 254 or over-coupled regime.

255 Having established the symmetries of the different polarization channels, we compare measured
 256 spatial intensity distributions with CWT, and extract the apparent coupling strength κ through
 257 a fitting procedure. At a fixed particle size but different array sizes we expect fixed values of
 258 coupling strength κ so that different array sizes ($L = 80 \mu\text{m}$, $60 \mu\text{m}$ and $40 \mu\text{m}$) allow us to verify
 259 the predicted influence on the spatial intensity distribution patterns by Eq. (2-3). As the coupling
 260 strength is only dependent on the size of the nanoparticles, we fit the data from all samples with
 261 the same particle diameter but different field sizes and polarizations simultaneously. Next, we
 262 expect that different coupling strength values are obtained as function of particle diameter (40

263 nm to 90 nm). To perform the fit we consider the solution of Eq. (3) for the lowest-threshold
 264 mode, and extract a unique mapping from the coupling coefficient κ to γ . By fitting Eq. (2) to the
 265 experimental result we obtain γ , which then translates into κ through the tabulated mapping. Note
 266 that this leaves some ambiguity since γ and $-\gamma$ are equivalent in the definition Eq. (2), while the
 267 intensity observables $|R \pm S|^2$ are agnostic to $\gamma \rightarrow \gamma^*$. Hence we in fact determine $|\text{Re} \kappa|$ and $|\text{Im} \kappa|$.

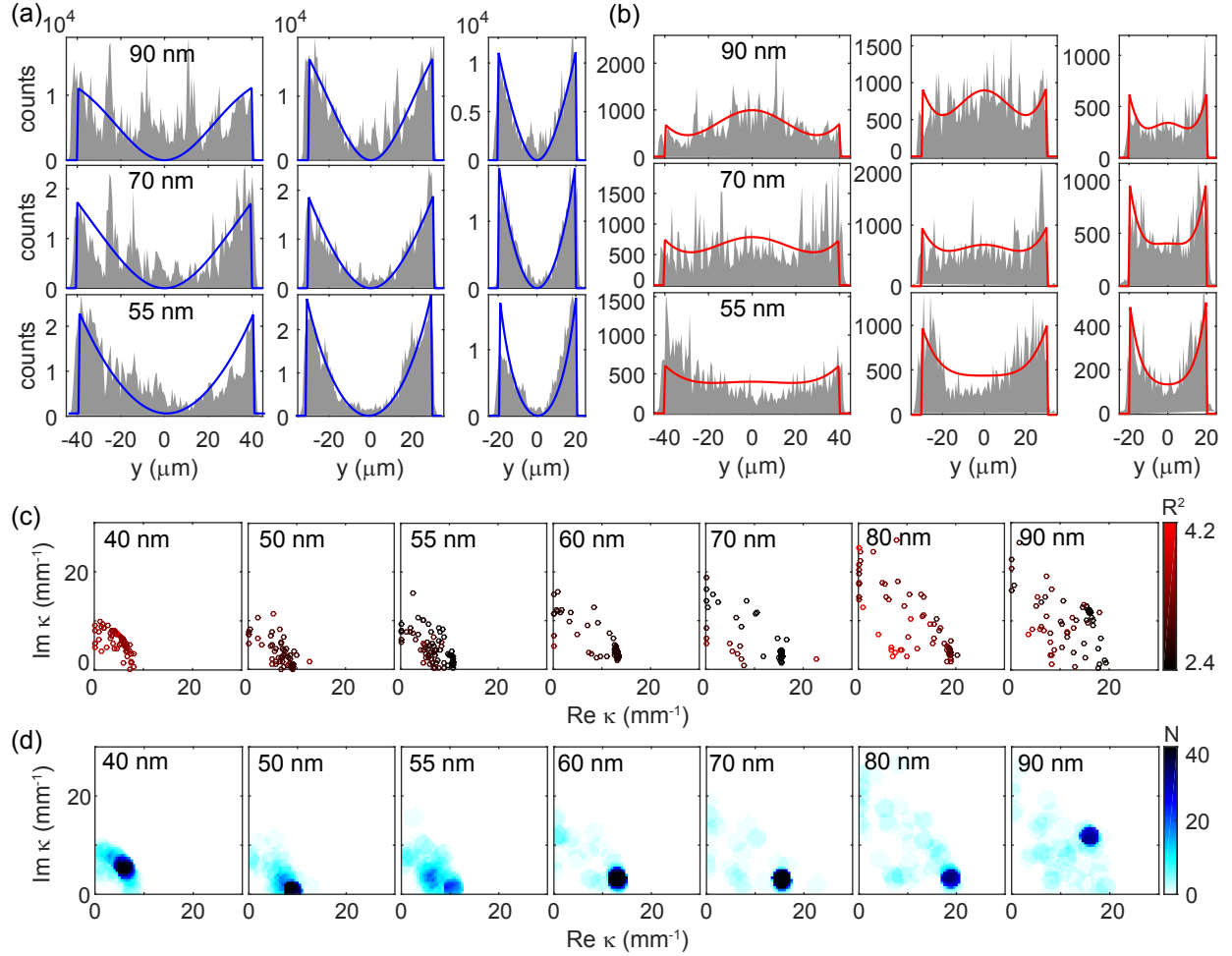


FIG. 5. Measured lasing intensity (gray) as function of y from samples with different particle sizes (columns) and field sizes (rows), overplotted with the fits (blue). (a): x -polarization; (b): y -polarization. The x -polarization results always show anti-symmetric profiles. The y -polarization results show a transition from under-coupled to over-coupled regime. Samples are excited by single shots, at around 6 times the threshold power. (c) We obtained values of κ by fitting to the measured spatial intensity profiles of arrays with different particles sizes, using different starting points for the fit. The color scale represents the result of histogramming the resulting fit values, with histogram entries weighted by the associated residual of the fit.

It is difficult to obtain robust fits of the envelope functions using least squares minimization due to the random speckles, which are effectively high-amplitude and high-spatial frequency noises that do not follow a Gaussian distribution. The blue and red solid lines in Fig. 5(a-b) show examples of fits, where all panels on the same row have been fitted simultaneously to a single parameter set. While there are some clear differences related to the speckle, overall the fitted curves represent well the measured intensity envelopes. As check of the fit procedure, we ran it with different starting values for κ evenly distributed in the first quadrant of the complex space within $|\kappa| < 0.03 \mu\text{m}^{-1}$ (under-coupled to over-coupled regime). Although the fit routine reports convergence at different values depending on the starting estimate, the lowest-residual results cluster in small regions in the complex plane. To determine the best global parameter estimate, we histogram the fitted values in discrete boxes in κ -space of 2 mm^{-1} width. Fig 5 (c) shows the resulting 2D histogram in the complex plane. The fitted κ cluster at distinct complex values, with $|\kappa|$ increasing with increasing particle size, as expected from the fact that larger Ag particles scatter more strongly. As best estimate for κ we take the average values over the densest bin.

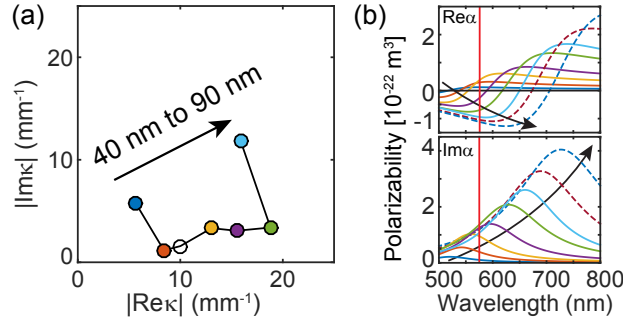


FIG. 6. (a) Value of κ for different particle diameters obtained by averaging over the densest bin (averaging radius of 2 mm^{-1}) in Fig. 5(c). Arrow indicates increase of particle diameter from 40 nm to 90 nm. (b) real and imaginary part of polarizability α as extracted by fitting calculated extinction in Ref. [49], Fig. 1b, for particle diameters 40 to 110 nm (10 nm steps, dashed lines for particle sizes not included in this experiment). Color coding of points in (a) matches lines in (b). Red vertical line: lasing condition at 575 nm.

Fig. 6(a) shows that the coupling constant $|\kappa|$ according to our measurement ranges from 5 to 20 mm^{-1} , i.e., $|\kappa/k_0| \approx 0.0003 - 0.0012$, with a systematic variation in the magnitude and phase of κ with particle size. These variations are not monotonic in e.g., particle volume, qualitatively consistent with the fact that the particle response as quantified by its polarizability is dispersive, with

its dispersive line shape sweeping through the laser condition as particle size is varied (Fig 6(b)). In magnitude the fitted κ -values are similar to those in conventional index-coupled DFB lasers[44] ($0 - 20 \text{ mm}^{-1}$), and surprisingly are much lower than expected from complex-coupled DFB lasers ($50 - 200 \text{ mm}^{-1}$) with metal gratings[50]. Also these values are significantly smaller than observed for surface plasmon lasers ($\kappa/k_0 = 0.012 - 0.017$) based on metal hole arrays[4, 5]. This is highly surprising because plasmonic lattice lasers have been reported to benefit from the strong coupling between light and metal nanoparticles[9, 42]. While holes in a metal film are not resonant scatterers, the metal nanoparticles in plasmon lasers have large resonant scattering cross sections. Intuitively, one would hence expect plasmon particle arrays to have higher coupling coefficients than metal hole arrays, opposite to the experimental findings.

V. INTERPRETATION OF FITTED COUPLING COEFFICIENTS

In this section we examine the values of the measured coupling coefficients from two perspectives. The first perspective derives from the fact that according to the standard derivation of CWT (Section I) the coupling coefficients simultaneously determine the real space profiles *and* the anticrossings in the photonic band structures. More particularly, κ in CWT directly determines the relative bandwidth of the stop gap in below-threshold band diagrams, while the magnitude of κ_{out} determines if the stop gap is asymmetric around the geometrical Bragg condition. Section V A examines the band structure. The second perspective is to compare measured coupling strengths to estimates of coupling coefficients from the geometry of our lasers using formulas common for (dielectric) DFB lasers [44] (section V B)

A. Coupling coefficients and band structure

Earlier reports on plasmon lattice lasers claimed 3% relative stop gap width in band structures. Hence one would expect $|\kappa/k_0| \approx 0.03$ instead of 0.0012. Here we compare the fitted values of $\text{Re}(\kappa)/G_y$ with the bandedge shifts measured from the investigated lasers, as well as those extracted from earlier work [12, 49]. We extract TE band edges from the below threshold emission spectra of the lasers at $k_x = k_y = 0$ (averaging over $|k_y| < 0.02k_0$ at $k_x = 0$) in x -polarized Fourier spectral images, shown as the color scale in Fig. 7(a). The spectral peaks are identified as two stop band edges (center frequencies plotted in Fig. 7(c)). This band, with its narrow bandwidth,

314 corresponds to the asymmetric lasing mode with nodes at the metal nanoparticles. The lower band
 315 edge has a much broader bandwidth and significantly shifts towards the red as particle diameter
 316 increases from 40 nm to 50 nm, and then disappears due to the broadening as the particle size
 317 further increases. We also simulated near-normal incidence transmission using an FEM method
 318 (COMSOL), taking 30 nm height Ag cylinders [51] on glass ($n = 1.50$) and in a $n = 1.60$ slab
 319 of 350 nm thickness. We choose slightly off-normal incidence (angle below 0.5°), as otherwise
 320 the coupling to the narrow band edge is forbidden by symmetry. The transmission (color scale
 321 in panel 7(b)) again shows distinct resonances, with a narrow band that hardly shifts and a lower
 322 band that redshifts and broadens with increasing particle size. The broadening of the lower band
 323 indicates increasing Ohmic and radiative loss, which may explain its vanishing in the fluorescence
 324 data. The small $\sim 0.3 \times 10^{15}$ rad/s shift in frequencies between measurement and simulations,
 325 likely owes to a small difference in waveguide mode index. The band at $\omega \sim 3.4 \times 10^{15}$ rad/s is a
 326 surface lattice resonance at the SU8-glass interface, which is irrelevant to the lasing experiment.

327 Figure 7(c) shows the shifts of the measured band edges from the theoretical band crossing
 328 point $\omega_0 = c/n_{\text{wg}}G_y$. To construct a "master diagram" that can also accommodate literature data
 329 sets alongside our measurements and that explicitly accounts for the plasmonic resonance of the
 330 particles, we convert particle size into a detuning parameter. This normalized detuning is defined
 331 as the difference between lasing frequency and the single-particle plasmon resonance frequency,
 332 divided by the single-particle plasmon resonance width. The single-particle properties were de-
 333 rived from scattering calculations (Fig. 6(b), Ref. 49). Alongside the band shifts in this work
 334 (closed blue and red points in Figure 7(c)), band edge shifts are shown for square lattices with the
 335 same gain medium as studied in this work, but much larger particles (Ref. 12, open diamonds)
 336 and samples with the lasing condition tuned far to the red by using a larger pitch and different
 337 gain medium (open circles[49]). The three datasets together cover red detuning [49], near-zero
 338 detuning, and blue detuning [12] and show important general features. The stop gap has one band
 339 edge that barely shifts from the geometric Bragg diffraction condition, and one band edge that
 340 shifts strongly. The shifting band shows a strong dependence on detuning from the plasmon res-
 341 onance, commensurate with the fact that it corresponds to the symmetric Bloch mode with field
 342 antinodes overlapping strongly with the particles. Notably, the shift increases when approaching
 343 the plasmon resonance, and its sign reverses at zero detuning. This behavior qualitatively traces
 344 out the real part of the dispersive particle polarizability. The band that hardly shifts corresponds to
 345 the antisymmetric mode with nodes at the particles, which is also the mode that lases in the experi-

ments. As earlier work [49] only examined the relative stop gap width (Figure 7(d)), it overlooked the large asymmetry in the two band shifts relative to ω_0 .

The coupling strength $|\text{Re}\kappa|/G_y$ that we derive from fitting the real space laser intensity profiles stays far below the half width of the band gap, and is similar in magnitude to the very small shift in frequency of the lasing band edge rather than to the stop gap width. This observation is surprising in framework of CWT. In CWT, strongly asymmetric band shifts require $|\text{Im}\kappa_{\text{out}}| \gg |\text{Re}\kappa_{\text{back}}|$. Yet if this inequality would indeed hold, the coupling strength evident in real space intensity distributions would be much larger than we observe, and would far exceed the shift of the upper band. Conversely, negligible shift of the lasing band edge and the small coupling strength obtained from real space profiles according to CWT dictate a negligible contribution of κ_{out} , incommensurate with the overall stop gap width. We conclude that the standard CWT fails to describe plasmon particle lasers consistently. The parameters needed to parametrize real space intensity distributions are not reconcilable with the plasmon band structure. We ascribe this to the fact that standard CWT assumes a perturbative plane wave expansion framework which very poorly accounts for the resonant and highly localized nature of the metal particles. This problem is also well known from the convergence-problems encountered by plane-wave based calculation methods for metal gratings [52]. At the same time, even if CWT fails to capture the band shifts, the fact that the lasing band shows an anomalously small shift is consistent with the coupling strength evident in the real space intensity distributions.

B. Geometry-based estimates

366

As second perspective on the measured coupling strengths we compare to estimates of coupling coefficients from the geometry of our lasers. For a waveguide geometry with dielectric perturbation and in the limit of particles much smaller in height than the scale on which the waveguide mode varies, the formalism of Kazarinov et al. [44] results in

$$\kappa_{\text{back}} \approx \left(\frac{1}{2G_y} \right) \left(\frac{\omega}{c} \right)^2 \epsilon_{02}(z_0) \phi(z_0)^2 h / \int \phi(z)^2 dz, \quad (4)$$

$$\kappa_{\text{out}} \approx - \left(\frac{1}{4G_y^2} \right) \left(\frac{\omega}{c} \right)^4 (\epsilon_{01}(z_0) \phi(z_0))^2 h^2 / \int \phi(z)^2 dz. \quad (5)$$

Here $h = 30$ nm is the thickness of the particles, $z_0 = 15$ nm is the height of the particle center and ϵ_{mn} signifies the 2D Fourier coefficient (at $(m,n)2\pi/d$) of the relative permittivity of the

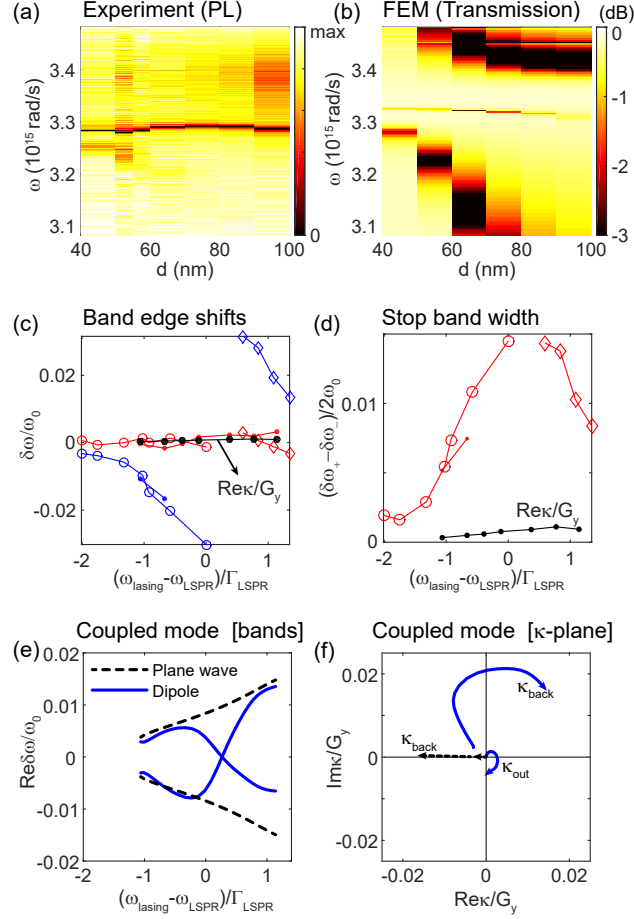


FIG. 7. (a) Measured below-threshold emission spectra versus particle diameter, near normal-incidence. (b) Zero-order transmittance obtained from FEM simulation. (c) Shift of the band edges (red: lasing band edge, blue: non-lasing band edge) relative to the Bragg condition, versus detuning between lasing condition and plasmon resonance. This graph combines data from this work (closed symbols) and Ref. [12, 49] (open symbols). Closed black symbols: coupling constant $\text{Re}\kappa/G_y$ (black) from Fig. 6. (d) Measured (half) band gap width (red, difference between red and blue points in panel (c)), alongside $\text{Re}\kappa/G_y$ (black). (e) Band shift and (f) coupling coefficients from CWT (black dashed curves, Eq. (4,5)) and dipole approximation (blue solid curves, Eq. 8,9). Arrows indicate increasing particle size.

369 scattering particles embedded in the waveguide background. The vertically stratified structure
 370 causes a weighting of the Fourier coefficients by the waveguide mode profile $\phi(z)$. The above
 371 expressions do not naturally relate to, e.g., the resonant dipole polarizability α of the localized
 372 plasmon scatterers. We turn Eq. (5) into one that does include α by following the approach of
 373 Spry and Kosan [53] and Vos et al. [54, 55] in the field of colloidal photonic crystals. Vos et

al. [54, 55] introduced a "photonic strength" Ψ that equals the relative stop gap width ($\Delta\omega/\omega$) and that for a 3D photonic crystal of spheres of radius R and polarizability α is expressed as

$$\Psi = 4\pi \frac{\alpha}{V} f(GR) \quad \text{with} \quad f(x) = \frac{j_1(x)}{x}. \quad (6)$$

This result is also well known in dynamical X-ray diffraction theory (limit of very small polarizabilities) [56]. In this equation, V is the unit cell volume, $\alpha = 3V_{\text{sphere}}(\epsilon_{\text{sphere}} - \epsilon_{\text{host}})/4\pi(\epsilon_{\text{sphere}} + 2\epsilon_{\text{host}})$, and $f(GR)$ is proportional to the Fourier transform of a sphere, with j_n the spherical Bessel function of the first kind, and G the length of the reciprocal lattice vector that causes the stop gap. The plane wave method for photonic crystals instead predicts [57]

$$\frac{\Delta\omega}{\omega} = \frac{\epsilon_G}{\bar{\epsilon}} = \frac{\epsilon_{\text{sphere}} - \epsilon_{\text{host}}}{\bar{\epsilon}} \frac{4\pi R^3}{V} f(GR), \quad (7)$$

where ϵ_G is the Fourier transform of the relative permittivity and $\bar{\epsilon}$ is the volume averaged relative permittivity. Note that Eq. 6 is different from Eq. 7, unless one substitutes $\alpha = 3V_{\text{sphere}}(\epsilon_{\text{sphere}} - \epsilon_{\text{host}})/4\pi(\epsilon_{\text{sphere}} + 2\epsilon_{\text{host}})$ for $V_{\text{sphere}}(\epsilon_{\text{sphere}} - \epsilon_{\text{host}})/4\pi\bar{\epsilon}$. Nonetheless, empirically Eq. (6) is a better predictor for band gaps in high index photonic crystals than Eq. (7), suggesting that Eq (6) accounts better for strong multiple scattering. Eq. (6) can be read as an Ansatz to convert Eq. (4,5). To this end, we evaluate the Fourier coefficients ϵ_{01} and ϵ_{02} , and replace any occurrence of $(\epsilon_{\text{disk}} - \epsilon_{\text{SU8}})/n_{\text{WG}}^2 V$ with $4\pi\alpha$, leading to

$$\frac{\kappa_{\text{back}}}{G_y} = \frac{4\pi\alpha}{V_{\text{eff}}} f(2GR), \quad (8)$$

$$\frac{\kappa_{\text{out}}}{k} = -kh_{\text{eff}} \left(\frac{4\pi\alpha}{V_{\text{eff}}} f(GR) \right)^2, \quad \text{with } f(x) = \frac{J_1(x)}{x}. \quad (9)$$

Now, the cylindrical Bessel function J_n appears and the effective unit cell volume V_{eff} is the product of the unit cell area and an effective waveguide mode height $h_{\text{eff}} = \int |\phi(z)|^2 dz / |\phi(z_0)|^2$.

Figure. 7(e-f) show expected coupling constants and band shifts using both the 'plane wave' result (Eq. (4,5)) and the modified 'dipole' result Eq. (9). For evaluation we use the polarizability at fixed wavelength (575 nm, the lasing wavelength) as extracted by matching to full-wave simulations for Ag particles in the glass-SU8-air system (Fig. 6(b)). In both models κ_{out} is much smaller than κ_{back} , and $|\kappa_{\text{back}}/G_y|$ reaches about 0.02, quite similar to the 3% relative stop gap width in Fig. 7(c-d), but exceeding by one order of magnitude the coupling coefficient obtained from real space intensity distributions. The major difference between the two models lies in the phase of the coupling coefficients, as only the dipole model captures the resonant dispersive behavior of α . On

391 a positive note, the model that uses the dipole polarizability well captures the dispersive behavior
392 of the band edge shifts, and the non-monotonic increase of the coupling coefficient with particle
393 size. However, there remains an important difference with the data, since both models predict
394 symmetric shifts around the Bragg condition as opposed to the observed non-shifting band.

395 To conclude, as was also observed for metal hole array lasers [4, 5] CWT parametrizes the
396 spatial intensity distributions in plasmon lattice lasers. However, in contrast to the behavior of
397 conventional DFBs as well as metal hole array lasers, the actual parameter-values are neither
398 internally consistent with the stopgaps observed in band structures nor reconcilable with simple
399 estimates on basis of the unit cell geometry. The common assumption underlying these consistency
400 checks is that CWT with its parameters can be derived from a plane wave expansion method.
401 However, plane wave expansion methods are notoriously poor for metal nanoparticle gratings,
402 rationalizing why CWT appears inconsistent with parameter estimates from geometry and with
403 measured stop bands in band structures.

404 VI. CONCLUSION

405 In this article, we quantified real space intensity distributions in plasmon antenna array plasmon
406 DFB lasers and showed that they can be well parametrized by the seminal CWT of Kogelnik and
407 Shank [43]. Notably, we trace the transition from under-coupled to over-coupled behavior as a
408 given particle array geometry is scaled in overall field size L , and can extract coupling strength
409 parameters that only depend on the choice of unit cell (i.e., particle size). This observation provides
410 an alternative explanation for the results of Hakala et al [14] who claimed "bright" and "dark"
411 lasing modes to be associated with dipole and quadrupolar particle resonances. Instead, the same
412 spatial profiles can arise from CWT as combined result of detection polarization, mode symmetry
413 and coupling strength, without resorting to any plasmonic resonance feature.

414 While CWT forms an effective parametrization, extracted coupling strengths are anomalously
415 small and inconsistent with parameter value estimates in the coupled wave framework. Viewing
416 CWT as a generic effective description of coupled forward and backward waves, it is not surprising
417 that it provides an effective parametrization. However, matching this description to photonic band
418 structure parameter estimates is essentially based on the assumption that the plane wave expansion
419 method, from which CWT derives, is accurate. Plane wave approximations are notorious for
420 performing poorly on strongly scattering plasmonic constituents [52]. The quantitative mismatch

421 between CWT coupling constants and data hence points at a fundamental shortcoming of coupled
422 wave modelling for strongly scattering periodic active systems.

423 Our result should be read as a stimulus to develop new theory. Many researchers currently focus
424 on collective effects, strong coupling and exciton-polariton physics in plasmon lattices. At the
425 same time active dielectric metasurfaces with gain are of increasing interest. For all these systems,
426 the unit cells are resonant, and hence the problem that we identify is acute. Ideally, models to
427 describe the physics of such systems should capture the unit cell physics in real space. However,
428 to our knowledge all available real-space models for such system with gain do not incorporate
429 noise to start the lasing process, and use Floquet periodic boundary conditions. It is hence a
430 formidable challenge to deal with finite systems. Our work provides clear observables against
431 which a model should be benchmarked, namely (1) band structures with relative wide stop bands
432 with asymmetric band shifts, (2) lasing thresholds with spatial intensity distributions mimicking
433 CWT predictions, (3) yet with anomalous coupling coefficients compared to the band structure. In
434 absence of such a model, one could pragmatically — but without any first-principles footing —
435 adopt CWT as parametrization on the understanding that *different* effective coupling coefficients
436 should be assigned to the two band edges. On basis of the interpretation of Hakala et. al. [14]
437 one could speculate that a main challenge is to identify coupling coefficients of various bands with
438 multipolar particle resonances.

439 ACKNOWLEDGMENTS

440 The authors thank Sachin Kasture, Martin van Exter, Mohammed Ramezani, Alexei Halpin
441 and Jaime Gomez Rivas for insightful discussions, and are grateful for Dimitry Lamers and Bob
442 Drenth for nanofabrication. Also, we thank Esther Alarcon Llado for suggestions to improve the
443 manuscript. This work is part of the research programme STW LEDMAP with project number
444 12754 which is (partly) financed by the Netherlands Organisation for Scientific Research (NWO).
445 It was performed at the research institute AMOLF.

446 Appendix A: Appendix - Spatial coherence

447 We confirmed transverse spatial coherence using double slit experiments. A pair of parallel
448 slits is placed in the intermediate image plane (center of the telescope, $50\times$ magnified image of

the sample). The slits are fabricated in chrome on glass (Delta Mask), with a width of 0.3 mm and center-center distance of 3 mm. Using a cylindrical lens ($f = 20$ mm) and relay optics, we obtain a two-slit interference pattern at the camera or spectrometer entrance plane. The resulting image is in one dimension a (magnified) Fourier transform of the product of laser emission and slits, and has spatial coordinate along the slit axis as horizontal coordinate. For full coherence and on the proviso of equal intensity through the slits, the image will have a fringe pattern in the y (k_y) direction that follows:

$$I(k_y) \propto \frac{\sin^2(k_y k_0 W/2)}{k_y^2} \cdot [1 + \cos(k_y k_0 D)], \quad (\text{A1})$$

with W the slit width and D the slit distance. If the laser emission selected by the two slits is only partially coherent with each other, a reduced fringe contrast v results

$$v = \frac{I_{\max} - I_{\min}}{I_{\max} + I_{\min}}. \quad (\text{A2})$$

Taking the $80 \mu\text{m} \times 80 \mu\text{m}$ lasers as representative example, we measured the coherence between two $6 \mu\text{m}$ wide slices that are $60 \mu\text{m}$ apart, each positioned near one edge of the sample. We took care to balance emission intensities by placing the slits symmetrically. Figure 8(a)(b) show the x polarized interference images measured with the CCD camera from the laser with particle diameter $d = 90$ nm, with the x - resp. y -direction of the laser aligned along the direction of the slits respectively. Clear interference fringes are only observed in the y direction. This indicates a strong spatial coherence in the y -direction, consistent with CWT for a laser with feedback along y only. To deduce the fringe contrast we eliminate the influence of spontaneous emission background and the TM waveguide mode of the lasers by spectral selection using the spectrometer. Figure 8(c) shows an example of a resulting spectrally filtered interference pattern ($d = 90$ nm laser, slice near $x = 0$) in two different polarization channels. Fitting the peaks and valleys with sinc functions (motivated by Eq. (A1) we obtain the fringe visibility. In x -polarization we find a visibility around 0.8, i.e., high coherence for all measured lasers. We attribute the fact that the measured visibility is below 1 mainly to the fact that any unbalance in the emission intensity transmitted through each slit reduces visibility, as may be caused by speckle or small misalignment. The y -polarization has a visibility that reduces from 0.7 to 0.4 as the particle size increases from 55 nm to 90 nm (from under-coupled to critically coupled regime). We expect this reduced contrast to reflect the fact that the y -polarized laser emission is generally weaker (for the TE mode), so that at any given background level, fringe contrast is less than for x -polarization. Indeed, the background is similar

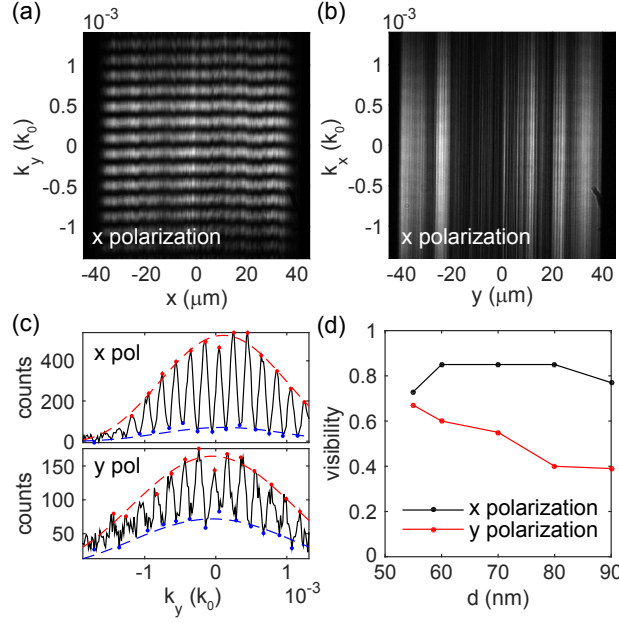


FIG. 8. (a-b) Double slit interference patterns for x -polarization with slits parallel to (a) x -direction and (b) y -direction. (c) Double slit interference patterns for (upper) x and (lower) y -polarizations at wavelength of the TE lasing mode, with peaks and valleys fitted to two sinc functions. (d) Visibilities of the x and y polarization of the TE mode obtained from the fit for lasers with different particle sizes. Laser size: $80 \mu\text{m} \times 80 \mu\text{m}$. (a-c): $d = 90 \text{ nm}$.

for the two polarizations in (c) (blue curve).

-
- [1] V. G. Kravets, A. V. Kabashin, W. L. Barnes, and A. N. Grigorenko, “Plasmonic surface lattice resonances: A review of properties and applications,” *Chem. Rev.* **118**, 5912–5951 (2018).
 - [2] G. Lozano, S. R. K. Rodriguez, M. A. Verschuuren, and J. G. Rivas, “Metallic nanostructures for efficient LED lighting,” *Light: Sci. Appl.* **5**, e16080 (2016).
 - [3] F. van Beijnum, P. J. van Veldhoven, E. J. Geluk, M. J. A. de Dood, G. W. ’t Hooft, and M. P. van Exter, “Surface plasmon lasing observed in metal hole arrays,” *Phys. Rev. Lett.* **110**, 206802 (2013).
 - [4] M. P. van Exter, V. T. Tenner, F. van Beijnum, M. J. A. de Dood, P. J. van Veldhoven, E. J. Geluk, and G. W. ’t Hooft, “Surface plasmon dispersion in metal hole array lasers,” *Opt. Express* **21**, 27422–27437 (2013).

- [5] V. T. Tenner, M. J. A. de Dood, and M. P. van Exter, “Measurement of the phase and intensity profile of surface plasmon laser emission,” *ACS Photonics* **3**, 942–946 (2016).
- [6] X. Meng, J. Liu, A. V. Kildishev, and V. M. Shalaev, “Highly directional spaser array for the red wavelength region,” *Laser Photonics Rev.* **8**, 896–903 (2014).
- [7] J. Stehr, J. Crewett, F. Schindler, R. Sperling, G. von Plessen, U. Lemmer, J.M. Lupton, T.A. Klar, J. Feldmann, A.W. Holleitner, M. Forster, and U. Scherf, “A low threshold polymer laser based on metallic nanoparticle gratings,” *Adv. Mater.* **15**, 1726–1729 (2003).
- [8] J. Y. Suh, C. H. Kim, W. Zhou, M. D. Huntington, D. T. Co, M. R. Wasielewski, and T. W. Odom, “Plasmonic bowtie nanolaser arrays,” *Nano Lett.* **12**, 5769–5774 (2012).
- [9] W. Zhou, M. Dridi, J. Y. Suh, C. H. Kim, D. T. Co, M. R. Wasielewski, G. C. Schatz, and T. W. Odom, “Lasing action in strongly coupled plasmonic nanocavity arrays,” *Nat. Nanotechnol.* **8**, 506–511 (2013).
- [10] A. Yang, T. B. Hoang, M. Dridi, C. Deeb, M. H. Mikkelsen, G. C. Schatz, and T. W. Odom, “Real-time tunable lasing from plasmonic nanocavity arrays,” *Nat. Commun* **6**, 6939 (2015).
- [11] A. Yang, Z. Li, M. P. Knudson, A. J. Hryn, W. Wang, K. Aydin, and T. W. Odom, “Unidirectional lasing from template-stripped two-dimensional plasmonic crystals,” *ACS Nano* **9**, 11582–11588 (2015).
- [12] A. H. Schokker and A. F. Koenderink, “Lasing at the band edges of plasmonic lattices,” *Phys. Rev. B* **90**, 155452 (2014).
- [13] M. Ramezani, A. Halpin, A. I. Fernández-Domínguez, J. Feist, S. R.-K. Rodriguez, F. J. García-Vidal, and J. G. Rivas, “Plasmon-exciton-polariton lasing,” *Optica* **4**, 31–37 (2017).
- [14] T. K. Hakala, H. T. Rekola, A. I. Väkeväinen, J.-P. Martikainen, M. Nečada, A. J. Moilanen, and P. Törmä, “Lasing in dark and bright modes of a finite-sized plasmonic lattice,” *Nat. Commun.* **8**, 13687 (2017).
- [15] H. T. Rekola, T. K. Hakala, and P. Törmä, “One-dimensional plasmonic nanoparticle chain lasers,” *ACS Photonics* (2018).
- [16] K. S. Daskalakis, A. I. Väkeväinen, J.-Petri Martikainen, T. K. Hakala, and P. Törmä, “Ultrafast pulse generation in an organic nanoparticle-array laser,” *Nano Lett.* **18**, 2658–2665 (2018).
- [17] S. R. K. Rodriguez, Y. T. Chen, T. P. Steinbusch, M. A. Verschuuren, A. F. Koenderink, and J. Gómez Rivas, “From weak to strong coupling of localized surface plasmons to guided modes in a luminescent slab,” *Phys. Rev. B* **90**, 235406 (2014).

- [18] A. I. Vokevinen, R. J. Moerland, H. T. Rekola, A.-P. Eskelinen, J.-P. Martikainen, D.-H. Kim, and P. Trm, “Plasmonic surface lattice resonances at the strong coupling regime,” *Nano Lett.* **14**, 1721–1727 (2014).
- [19] Tommi K. Hakala, Antti J. Moilanen, Aaro I. Vakevainen, Rui Guo, Jani-Petri Martikainen, Konstantinos S. Daskalakis, Heikki T. Rekola, Aleksi Julku, and Paivi Torma, “Bose-einstein condensation in a plasmonic lattice,” *Nature Phys.* **14**, 739 (2018).
- [20] S. T. Ha, Y. Hsing Fu, N. K. Emani, Z. Pan, R. M. Bakker, R. Paniagua-Dominguez, and A. I. Kuznetsov, “Directional lasing in resonant semiconductor nanoantenna arrays,” *Nature Nanotechn.*, in press DOI 10.1038/s41565-018-0245-5 (2018).
- [21] D. J. Bergman and M. I. Stockman, “Surface plasmon amplification by stimulated emission of radiation: Quantum generation of coherent surface plasmons in nanosystems,” *Phys. Rev. Lett.* **90**, 027402 (2003).
- [22] J. B. Khurgin, “Prospects and merits of metal-clad semiconductor lasers from nearly UV to far IR,” *Opt. Express* **23**, 4186–4194 (2015).
- [23] R. F. Oulton, V. J. Sorger, T. Zentgraf, R.-M. Ma, C. Gladden, L. Dai, G. Bartal, and X. Zhang, “Plasmon lasers at deep subwavelength scale,” *Nature* **461**, 629–632 (2009).
- [24] X. Meng, A. V. Kildishev, K. Fujita, K. Tanaka, and V. M. Shalaev, “Wavelength-tunable spasing in the visible,” *Nano Lett.* **13**, 4106–4112 (2013).
- [25] M. I. Stockman, “The spaser as a nanoscale quantum generator and ultrafast amplifier,” *J. Opt.* **12**, 024004 (2010).
- [26] D. A. Genov, R. F. Oulton, G. Bartal, and X. Zhang, “Anomalous spectral scaling of light emission rates in low-dimensional metallic nanostructures,” *Phys. Rev. B* **83**, 245312 (2011).
- [27] T. P. H. Sidiropoulos, R. Röder, S. Geburt, O. Hess, S. A. Maier, C. Ronning, and R. F. Oulton, “Ultrafast plasmonic nanowire lasers near the surface plasmon frequency,” *Nat. Phys.* **10**, 870876 (2014).
- [28] R.-M. Ma, R. F. Oulton, V. J. Sorger, G. Bartal, and X. Zhang, “Room-temperature sub-diffraction-limited plasmon laser by total internal reflection,” *Nat. Mater.* **10**, 110–113 (2011).
- [29] M. T. Hill, Y.-S. Oei, B. Smalbrugge, Y. Zhu, T. de Vries, P. J. van Veldhoven, F. W. M. van Otten, T. J. Eijkemans, J. P. Turkiewicz, H. de Waardt, E. J. Geluk, S.-H. Kwon, Y.-H. Lee, R. Nötzel, and M. K. Smit, “Lasing in metallic-coated nanocavities,” *Nat. Photonics* **1**, 589–594 (2007).

- [30] M. T. Hill, M. Marell, E. S. P. Leong, B. Smallbrugge, Y. Zhu, M. Sun, P. J. van Veldhoven, E. J. Geluk, F. Karouta, Y.-S. Oei, R. Nötzel, C.-Z. Ning, and M. K. Smit, “Lasing in metal-insulator-metal sub-wavelength plasmonic waveguides,” *Opt. Express* **17**, 11107–11112 (2009).
- [31] K. Yu, A. Lakhani, and M. C. Wu, “Subwavelength metal-optic semiconductor nanopatch lasers,” *Opt. Express* **18**, 8790–8799 (2010).
- [32] M. P. Nezhad, A. Simic, O. Bondarenko, B. Slutsky, A. Mizrahi, L. Feng, V. Lomakin, and Y. Fainman, “Room-temperature subwavelength metallo-dielectric lasers,” *Nat. Photonics* **4**, 395–399 (2010).
- [33] J. H. Lee, M. Khajavikhan, Q. Simic, A. and Gu, O. Bondarenko, B. Slutsky, M. P. Nezhad, and Y. Fainman, “Electrically pumped sub-wavelength metallo-dielectric pedestal pillar lasers,” *Opt. Express* **19**, 21524–21531 (2011).
- [34] M. Khajavikhan, A. Simic, M. Katz, J. H. Lee, B. Slutsky, A. Mizrahi, V. Lomakin, and Y. Fainman, “Thresholdless nanoscale coaxial lasers,” *Nature* **482**, 204–207 (2012).
- [35] H. Kogelnik and C. V. Shank, “Stimulated emission in a periodic structure,” *Appl. Phys. Lett.* **18**, 152–154 (1971).
- [36] B. E. Kruschwitz and T. G. Brown, “Complex-coupled distributed feedback laser with negative differential coupling,” *Appl. Phys. Lett.* **67**, 461–463 (1995).
- [37] G. A. Turnbull, P. Andrew, M.J. Jory, W. L. Barnes, and I. D. W. Samuel, “Relationship between photonic band structure and emission characteristics of a polymer distributed feedback laser,” *Phys. Rev. B* **64**, 125122 (2001).
- [38] G. Heliotis, R. D. Xia, G. A. Turnbull, P. Andrew, W. L. Barnes, I. D. W. Samuel, and D. D. C. Bradley, “Emission characteristics and performance comparison of polyfluorene lasers with one- and two-dimensional distributed feedback,” *Adv. Funct. Mater.* **14**, 91–97 (2004).
- [39] I. D. W. Samuel and G. A. Turnbull, “Organic semiconductor lasers,” *Chem. Rev.* **107**, 1272–1295 (2007).
- [40] H. Matsubara, S. Yoshimoto, H. Saito, Y. Jianglin, and S. Tanaka, Y. and Noda, “Gan photonic-crystal surface-emitting laser at blue-violet wavelengths,” *Science* **319**, 445–447 (2008).
- [41] A. H. Schokker and A. F. Koenderink, “Lasing in quasi-periodic and aperiodic plasmon lattices,” *Optica* **3**, 686–693 (2016).
- [42] A. H. Schokker and A. F. Koenderink, “Statistics of randomized plasmonic lattice lasers,” *ACS Photonics* **2**, 1289–1297 (2015).

- [43] H. Kogelnik and C. V. Shank, “Coupled-wave theory of distributed feedback lasers,” *Journal of Applied Physics* **43**, 2327–2335 (1972).
- [44] R. Kazarinov and Henry C., “Second-order distributed feedback lasers with mode selection provided by first-order radiation losses,” *IEEE J. Quantum Electron.* **21**, 144–150 (1985).
- [45] K. Sakai, E. Miyai, and S. Noda, “Two-dimensional coupled wave theory for square-lattice photonic-crystal lasers with tm-polarization,” *Opt. Express* **15**, 3981–3990 (2007).
- [46] M. Koba and P. Szczepanski, “The threshold mode structure analysis of the two-dimensional photonic crystal lasers,” *Prog. Electromagn. Res.* **125**, 365–389 (2012).
- [47] Y. Liang, C. Peng, K. Sakai, S. Iwahashi, and S. Noda, “Three-dimensional coupled-wave analysis for square-lattice photonic crystal surface emitting lasers with transverse-electric polarization: finite-size effects,” *Opt. Express* **20**, 15945–15961 (2012).
- [48] H. P. Urbach and G. L. J. A. Rikken, “Spontaneous emission from a dielectric slab,” *Phys. Rev. A* **57**, 3913–3930 (1998).
- [49] A. H. Schokker, F. van Riggelen, Y. Hadad, A. Alú, and A. F. Koenderink, “Systematic study of the hybrid plasmonic-photonic band structure underlying lasing action of diffractive plasmon particle lattices,” *Phys. Rev. B* **95**, 085409 (2017).
- [50] M. Kamp, J. Hofmann, F. Schäfer, M. Reinhard, M. Fischer, T. Bleuel, J. Reithmaier, and A. Forchel, “Lateral coupling as a material independent way to complex coupled dfb lasers,” *Opt. Mater.* **17**, 19 – 25 (2001).
- [51] P. B. Johnson and R. W. Christy, “Optical constants of the noble metals,” *Phys. Rev. B* **6**, 4370–4379 (1972).
- [52] L. Li and C. W. Haggans, “Convergence of the coupled-wave method for metallic lamellar diffraction gratings,” *J. Opt. Soc. Am. A* **10**, 1184–1189 (1993).
- [53] R. J. Spry and D. J. Kosan, “Theoretical analysis of the crystalline colloidal array filter,” *Appl. Spectr.* **40**, 782–784 (1986).
- [54] W. L. Vos, R. Sprik, A. van Blaaderen, A. Imhof, A. Lagendijk, and G. H. Wegdam, “Strong effects of photonic band structures on the diffraction of colloidal crystals,” *Phys. Rev. B* **53**, 16231–16235 (1996).
- [55] W. L. Vos, M. Megens, C. M. van Kats, and P. Bösecke, “Transmission and diffraction by photonic colloidal crystals,” *J. Phys.-Cond. Matt.* **8**, 9503–9507 (1996).
- [56] W. H. Zachariasen, *Theory of X-ray diffraction in crystals* (Dover Publications, 1945).

609 [57] H. S. Sözüer, J. W. Haus, and R. Inguva, “Photonic bands: Convergence problems with the plane-wave
610 method,” Phys. Rev. B **45**, 13962–13972 (1992).